

THUDose_{PD}: a three-dimensional Monte Carlo platform for phantom dose assessment*

Xi-Yu Luo,^{1,2} Rui Qiu,^{1,2} Zhen Wu,^{1,3,†} Shu-Chang Yan,^{1,2} Zi-Yi Hu,^{1,2} Hui Zhang,^{1,2} and Jun-Li Li^{1,2}

¹Department of Engineering Physics, Tsinghua University, Beijing 100084, China

²Key Laboratory of Particle and Radiation Imaging, Tsinghua University, Ministry of Education, Beijing 100084, China

³Nuctech Company Limited, Beijing 100084, China

Monte Carlo simulations are frequently utilized in radiation dose assessments. However, many researchers find the prevailing computing platforms to be intricate. This highlights a pressing need for a specialized framework for phantom dose evaluation. To address this gap, we developed a user-friendly radiation dose assessment platform using the Monte Carlo toolkit, Geant4. The Tsinghua University Phantom Dose (THUDose_{PD}) augments the flexibility of Monte Carlo simulations in dosimetric research. Originating from THUDose, a code with generic, functional, and application layers, THUDose_{PD} focuses predominantly on anatomical phantom dose assessment. Additionally, it enables medical exposure simulation, intricate geometry creation, and supports both three-dimensional radiation dose analysis and phantom format transformations. The system operates on a multi-threaded parallel CPU architecture, with some modules enhanced for GPU parallel computing. Benchmark tests on the ICRP reference male illustrated the capabilities of THUDose_{PD} in phantom dose assessment, covering the effective dose, three-dimensional dose distribution, and three-dimensional organ dose. We also conducted a voxelization conversion on the polygon mesh phantom, demonstrating the method's efficiency and consistency. Extended applications based on THUDose_{PD} further underline its broad adaptability. This intuitive, three-dimensional platform stands out as a valuable tool for phantom radiation dosimetry research.

Keywords: Monte Carlo, phantom, dose assessment, voxelization, three dimensional

I. INTRODUCTION

With the growing adoption of nuclear techniques in radiation protection and medical physics[1–6], accurate dose calculations for human phantoms have become indispensable. Phantom-dose evaluations are pivotal in clinical practices such as radiotherapy, CT irradiation, X-ray radiography, and in radiation protection undertakings such as retrospective dose reconstruction and epidemiological studies [7–9]. Among the myriad techniques available, the Monte Carlo algorithm is esteemed as the gold standard for dose computation. This method encapsulates all physical processes and offers insights into transport processes by emulating particle-matter interactions[10]. Furthermore, the Monte Carlo approach facilitates the translation of microscopic mechanisms into macroscopic doses and exhibits higher precision over analytical algorithms, especially in heterogeneous geometries.

Many specialized Monte Carlo software tools are dedicated to phantom dose calculations, including GATE[11, 12], TOPAS[13, 14], and ARCHER[15–17]. Each has been meticulously researched and optimized for specific application domains. Other notable methods in this arena are MCNPX[18], FLUKA[19], and Geant4[20]. While MCNPX and FLUKA largely operate via input card simulations, presenting a considerable workload for intricate geometries and source modeling, Geant4 stands out. Geant4 can accommodate more

complex geometries and offers an extensive suite of functionalities, enhancing code flexibility. Written in C++, this open-source platform facilitates easier packaging and further development.

Geant4's flexibility leads to complexity. Writing and debugging code for a novel simulation requires considerable effort, and it can be difficult for researchers without significant programming experience. Additionally, although Geant4 supports phantom dose calculations, the user should import the geometry, dose algorithm, and tally score. If Geant4 can be packaged, then a specific function can be connected to the interface parameters, and a convenient and stable phantom dose calculation platform can be generated for specific phantom dose calculations.

Therefore, we developed a dedicated phantom dose calculation platform, THUDose_{PD}, based on the Geant4 toolkit, which includes the following:

- preserve the underlying Geant4 code
- visual user interface
- provide various usage of phantom dose calculations
- support CPU and GPU multi-threaded parallel computing
- support three-dimensional visualization of geometry and results

The platform THUDose_{PD} is tailored for pragmatic applications in clinical medicine and radiation protection. It boasts a user-friendly interface that facilitates complex geometric modeling and supports the transport of electrons, photons, neutrons, protons, and heavy ions. Additionally, the platform accommodates both single and dual phantom dose calculations, catering to the routine needs of medical physics and radiation protection. It offers methodologies for evaluating

* Supported by the National Natural Science Foundation of China (General Program) (12175114, U2167209), the Foundation of Key Laboratory of Metrology and Calibration Technology (JLKG2022001C001), the Platform Development foundation of China Institute for Radiation Protection (YP21030101), the National Key R&D Program of China (2021YFF0603600), and the Tsinghua University Initiative Scientific Research Program (20211080081).

† Corresponding author, wuzhen97@tsinghua.org.cn

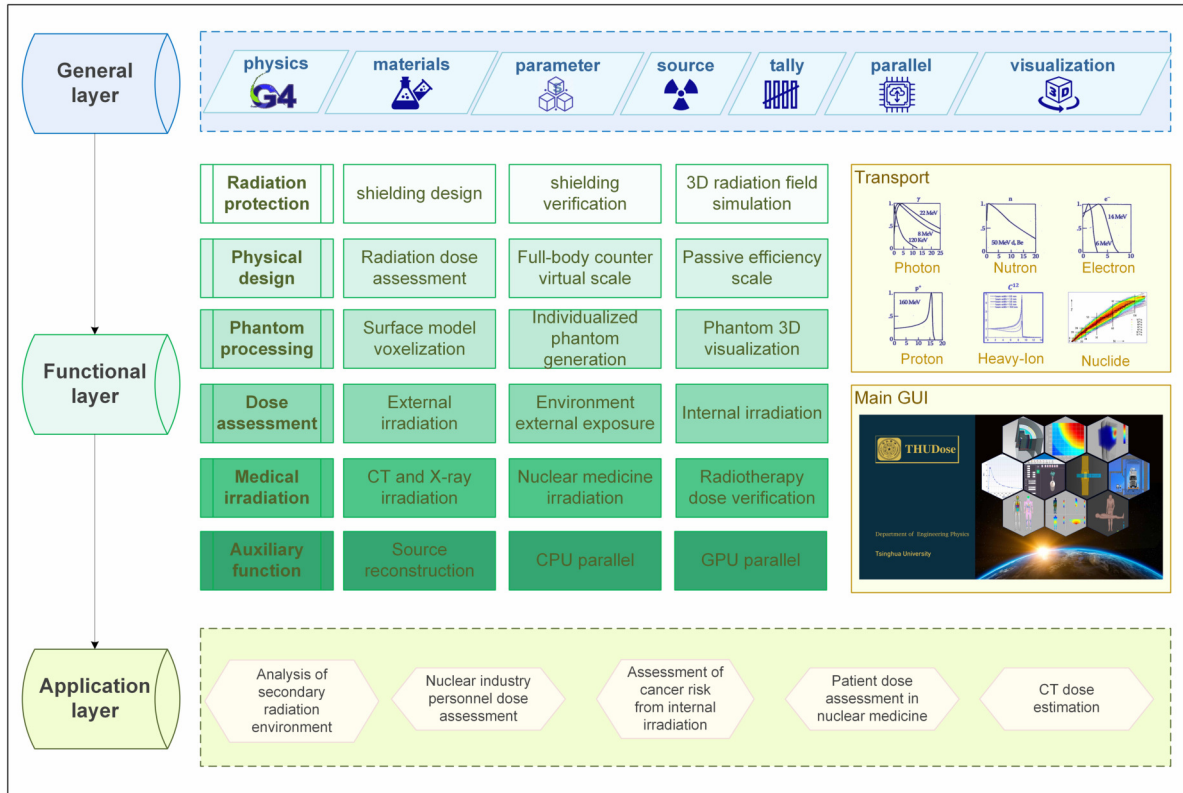


Fig. 1. The overall structure of THUDose platform.

58 organ doses from both external and internal exposures. Keeping
 59 in sync with the evolution of phantoms, THUDosePD
 60 has implemented a procedure for the voxelization of polygon-
 61 mesh phantoms. The platform further enhances user experi-
 62 ence by supporting three-dimensional visualization, spanning
 63 from the initial modeling phase to the final output. Grounded
 64 in a robust software architecture, THUDosePD has proven its
 65 merit in multiple research endeavors, covering scenarios of
 66 utmost interest to the majority of users and consistently offer-
 67 ing convenience and stability.

68

II. MATERIAL AND METHODS

69 The THUDosePD platform is based on THUDose[21], and
 70 was then expanded and developed for phantom dose calcula-
 71 tion and three-dimensional visualization. The extended pro-
 72 gram has additional features, such as creating and converting
 73 phantoms, pre-defining standard source types, external and
 74 internal irradiation dose algorithms, and geometry visualiza-
 75 tion.

76

A. The universal MC program THUDose

77 THUDose is an in-house general Monte Carlo procedure
 78 written in C++ that wraps and extends the Geant4 toolkit.

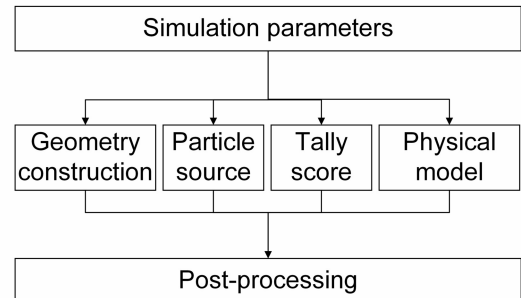


Fig. 2. The interactive interface organization structure of THUDose.

79 The platform operates via a Graphical User Interface (GUI)
 80 through which projects are built. In the background, XML
 81 files were saved using the settings set by the interface. The
 82 general, function, and application layers are the three layers
 83 that constitute THUDose. Figure 1 illustrates the system's
 84 overall structure. The four steps comprise a simulation in
 85 THUDose: geometric data, source definition, tally scores,
 86 and run parameters. The accompanying Figure 2 shows
 87 the organizational structure of the interactive interface and a
 88 schematic.

89 In THUDose, the developers integrated physics lists de-

90 rived from the cross-sectional libraries of both Geant4 and
 91 ENDF, selecting hadron and electromagnetic physics models
 92 for registration. This program was used to assess the trans-
 93 port of electrons, photons, protons, and neutrons. For material
 94 construction optimization, the platform provides two distinct
 95 strategies: The first approach utilizes the "Periodic Table" in-
 96 terface, allowing users to define materials on an individual
 97 basis. As an alternative, users can employ an Excel spread-
 98 sheet to craft a bill of materials, which facilitates the addition
 99 of materials in batches.

100 The source definition in THUDose is versatile, accommo-
 101 dating any particle type, energy, orientation, or spatial dis-
 102 tribution. It allows the creation of multiple tallies for a sin-
 103 gle project, with each tally functioning independently. The
 104 software diligently logs energy deposition, flux, and particle
 105 count in the medium, segmented by particle type. To boost
 106 computational efficiency, the developers integrated parallel
 107 computing modules based on MPI. At present, THUDose can
 108 utilize up to 2000 parallel computing cores, contingent upon
 109 the computer's memory capacity. Furthermore, the software
 110 is equipped with GPU parallel computing functionalities for
 111 electrons and photons[8, 22]. The team plans to introduce
 112 support for GPU-based proton transport in the near future.

113 B. Extensions for phantom dose assessment

114 Four processes comprise the majority of MC-based
 115 phantom dose assessments: phantom construction, parti-
 116 cle transportation, dose calculation algorithm, and visu-
 117 alization. We investigated these four areas and devel-
 118 oped a three-dimensional phantom dose assessment platform,
 119 THUDose_{PD} based on THUDose.

120 1. Phantom construction and conversion

121 Currently, the voxel phantom stands as the predominant hu-
 122 man anatomy model employed in radiation dose assessment.
 123 For precise dose assessment in intricate workplaces, it is vital
 124 to produce phantoms that offer adjustable sizes and postures.
 125 Such malleable models can be crafted using the Boundary
 126 Representation (BREP) geometric definition methods, which
 127 can take the form of nonuniform rational B-splines (NURBS),
 128 polygon meshes, or a combination thereof. Relative to voxel
 129 models, the BREP model offers a broader range of deforma-
 130 tion operations. It can represent new anatomical structures for
 131 staff or patients even in the absence of comprehensive whole-
 132 body image data[23]. For the purpose of this work, all BREP
 133 models, which are expressed as polygon-mesh phantoms be-
 134 fore final computations, are termed 'polygon-mesh phantom'.

135 Direct calculations on polygon mesh phantoms are unfea-
 136 sible. Typically, they are converted into either voxels or
 137 tetrahedrons to facilitate particle transport[24, 25]. As of
 138 now, THUDose_{PD} supports two such conversion techniques.
 139 However, given that tetrahedralization is not the focal point
 140 of this study, only the voxelization process is elucidated.

141 For the voxel phantom, THUDose_{PD} can import data in a
 142 binary file format. Pertinent files include both a configuration
 143 file and binary file. Details, such as phantom's size, voxel's
 144 resolution, and phantom's central coordinates, are specified
 145 in the configuration file. Each voxel's value corresponds to a
 146 material index within a predefined list, indicating its material
 147 classification.

148 For polygon-mesh phantoms, THUDose_{PD} offers a trans-
 149 formation procedure, termed voxelization. This method con-
 150 verts a three-dimensional object's geometric representation
 151 into a voxel format that closely mirrors the original. The
 152 resulting data captures both the surface and the inner geo-
 153 metric details. For rapid voxelization, THUDose_{PD} employs
 154 OpenGL and utilizes the fragment shader in the rendering
 155 process to transition the intersection of triangles and voxels
 156 into sampling points. In parallel, computing techniques expe-
 157 dite the voxelization outcomes.

158 To enhance clinical efficacy, precise radiation dose evalua-
 159 tions based on actual patient CT scans are paramount. To this
 160 end, a phantom construction module was developed to load
 161 DICOM files, extract HU values, and subsequently transform
 162 them into densities and materials for ensuing calculations.

163 2. Particle transportation and source definition

164 The THUDose_{PD} physical process is based on the THU-
 165 Dose physical model, facilitating the simulation and transport
 166 of photons, electrons, neutrons, protons, and heavy ions. The
 167 program has predefined the eight irradiation types highlighted
 168 in ICRU Publication 95: antero-posterior (AP), posterior
 169 anterior (PA), left lateral (LLAT), right lateral (RLAT), ro-
 170 tational (ROT), isotropic (ISO), superior hemisphere semi-
 171 isotropic (SS-ISO), and inferior hemisphere semi-isotropic
 172 (IS-ISO). For X-ray radiography, which is prevalent in med-
 173 ical applications, the source has been parameterized. Users
 174 simply define the source axis distance, deflection angle, and
 175 field size to initiate vertebral tract sampling. In the context
 176 of CT, a butterfly filter specific to CT machines was devel-
 177 oped to introduce a CT source[26]. Additionally, the program
 178 supports phase-space files for radiation field simulations and
 179 user-defined source parameters. Beyond these external ex-
 180 posure scenarios, the software offers two methodologies for
 181 internal exposure dose assessment: a swift computation ap-
 182 proach based on specific absorbed fraction (SAF) values de-
 183 termined via the Monte Carlo algorithm and a more detailed
 184 method reliant on the nuclide spectrum.

185 3. Dose calculation algorithms

186 The software offers three calculation modes: external, in-
 187 ernal, and environmental external radiation dose assessments
 188 [27]. Each mode facilitates computations of organ dose, ef-
 189 fective dose, and three-dimensional dose distribution. Organ
 190 doses can be directly calculated by utilizing voxels for Monte
 191 Carlo transport. Furthermore, to support three-dimensional
 192 radiation dose evaluations, THUDose_{PD} offers both voxel

193 tally and mesh tally modes. In the voxel tally mode, when
 194 the input geometry is presented in voxels, the software gen-
 195 erates a three-dimensional matrix identical in size to the ge-
 196 ometry. It records physical quantities in each voxel grid and
 197 saves them in the respective element of the output matrix.
 198 This output matrix represents the three-dimensional statisti-
 199 cal outcomes of the required physical quantities. Addi-
 200 tionally, when there is a discrepancy between geometric and tally
 201 resolutions, data can be documented in the mesh tally mode,
 202 which derives from the G4MeshKernelRect class.

203 The calculations for organ and effective doses occur in the
 204 dose assessment module, termed as dose postprocessing. The
 205 aim here is to ascertain radiation-sensitive organ doses and
 206 then compute the effective dose, taking into account the tissue
 207 weight factor. Moreover, the software includes dose conver-
 208 sion coefficient computing capabilities, offering a theoretical
 209 foundation for radiation protection dose evaluations.

210 Assessing the dose for the red bone marrow is both vi-
 211 tal and challenging in external radiation dose evaluations.
 212 THUDose_{PD} adopts distinct methodologies for dose compu-
 213 tations for typical organs and the red bone marrow. For organs
 214 excluding the red bone marrow, an average dose methodology
 215 is employed, as detailed in equations (1-2):

$$216 \quad D = \frac{d\bar{\epsilon}}{dm}, \quad (1) \quad 254$$

$$217 \quad D_T = \frac{1}{m_T} \int_{m_T} D dm, \quad (2) \quad 255$$

218 where $d\bar{\epsilon}$ denotes the mean energy imparted by ionizing
 219 radiation to matter of mass dm , D denotes the absorbed dose,
 220 and m_T denotes the mass of an organ or tissue. These two
 221 equations were used to calculate the average absorbed dose of
 222 organ T, D_T . Furthermore, THUDose_{PD} was used to directly
 223 count the energy deposition to obtain the absorbed dose of the
 224 organs with the exception of the red marrow and endosteum.

225 For the red bone marrow, THUDose_{PD} provides three
 226 evaluation methods.

227 **Direct method:** The approach considers the average dose of
 228 bones containing red marrow as the representative dose
 229 for the red marrow itself, termed as the bone-specific
 230 weighted average dose. This is computed as per the
 231 following formula, equation (3):

$$232 \quad D_{RBM} = \frac{E_{RBM}}{m_{RBM}} = \frac{E_{Bone} \times r_{RBM}}{m_{RBM}} \quad (3) \quad 264$$

233 The variable D_{RBM} represents the absorbed dose of
 234 the red bone marrow, while m_{RBM} signifies the mass
 235 of the red bone marrow. E_{RBM} and E_{bone} denote the
 236 energy deposits in the red bone marrow and bone, re-
 237 spectively. Lastly, r_{RBM} stands for the mass ratio of
 238 the red bone marrow to the bone.

239 **3CFs-improved method:** Given that the equilibrium condi-
 240 tion between the red bone marrow and trabecular bone
 241 is not met in phantoms, the S factor (or KS factor) is
 242 employed to calculate the dose of voxelized red bone
 243 marrow, termed the 3CFs method. Liu et al.[28] later
 244 refined this approach, resulting in the 3CFs-improved
 245 method. The absorbed dose D_{RBM} for the overall red
 246 bone marrow is the mass-weighted average of the red
 247 bone marrow dose at various locations. The associated
 248 formulas are presented in equation (4):

$$250 \quad D_{RBM}^i = D_{SPA}^i \cdot \frac{\int \left(\frac{\mu_{en}}{\rho} (E) \right)_{RBM} \phi(E) KS(E) E \cdot dE}{\int \left(\frac{\mu_{en}}{\rho} (E) \right)_{SPA} \phi(E) E \cdot dE} \quad (4)$$

251 where D_{RBM}^i and D_{SPA}^i denote the absorbed doses
 252 of the red bone marrow and spongiosa in bone i, the
 253 KS factor adopts the KS data of 44-year-old adults, E
 254 and $\phi(E)$ denote the photon energy and fluence in the
 255 spongiosa, respectively.

$$256 \quad \bar{D}_{RBM} = \sum_i R^i \cdot D_{RBM}^i \quad (5)$$

257 The final average dose to the total red marrow is pro-
 258 vided by equation (5), where R^i denotes the ratio of
 259 the mass of red marrow in bone i to the total mass of
 260 red marrow.

261 **Dose-response function method:** calculated with dose-
 262 response function method[29], as follows, equation
 263 (6-7):

$$264 \quad D(r_T, x) = \int_E \Phi(E, r_S, x) R(r_T \leftarrow r_S, x, E) dE, \quad (6)$$

$$265 \quad D_{skel}(r_T) = \sum_x \frac{m(r_T, x)}{m(r_T)} D(r_T, x). \quad (7)$$

266 Bone-specific absorbed dose per particle fluence ($Gy \cdot$
 267 cm^2) to red bone marrow and endosteum is a function
 268 of particle energy and skeletal region, i.e., $R(r_T \leftarrow$
 269 $r_S, x, E)$ in equation (6). The fluence of particles
 270 of energy E in the source tissue r_S of bone site x ,
 271 $\Phi(E, r_S, x)$, was simulated by THUDose_{PD}. The ab-
 272 sorbed dose to tissue r_T (red bone marrow) at bone
 273 site x was calculated using equation (6). Addition-
 274 ally, equation (7) is used to obtain the average absorbed
 275 dose of red marrow, where $m(r_T, x)$ and $m(r_T)$ denote
 276 the mass of tissue r_T at bone site x and the total mass
 277 of r_T , respectively.

276 For internal radiation dose computation, the software offers
 277 a quick estimation mode grounded on SAF values alongside
 278 a more detailed computation mode. The detailed approach
 279 utilizes Monte Carlo simulation, relying on the organ's nu-
 280 clide spectrum. This strategy accommodates various models,
 281 working positions, and nuclide residence durations, employ-
 282 ing the organ nuclide spectrum for the Monte Carlo simu-
 283 lation. Subsequently, the software calculates the equivalent
 284 and effective doses committed to the organs irradiated within
 285 the phantom. However, given this aspect is beyond the main
 286 scope of this research, it will not be extensively discussed
 287 here.

288 4. Three-dimensional visualization

289 THUDose facilitates the visualization of geometry and par-
 290 ticle trajectories in the 'wrl' format, compatible with most
 291 three-dimensional software. Moreover, THUDose_{PD} en-
 292 hances the three-dimensional visualization module, offering
 293 windows in four distinct views: perspective, front, side, and
 294 top. This advanced view supports the customization of vis-
 295 ible slices and adjusts the displayed dose value ranges. For
 296 CAD geometries and polygon-mesh phantoms, THUDose_{PD}
 297 allows imports in the 'ply' format and offers the ability to
 298 display components in a variety of colors. When it comes
 299 to voxel phantoms, THUDose_{PD} features a display func-
 300 tion for binary formats, where each organ can be distinc-
 301 tively showcased using a unique color set. In the realm of
 302 dose assessment, it is often pivotal to merge the geometry
 303 (or phantom) with the dose distribution, aiding in pinpoint-
 304 ing high-dose locations and facilitating radiation risk analy-
 305 ses. THUDose_{PD}'s visualization module presents a solution
 306 that concurrently visualizes both geometry and dose distribu-
 307 tion. The integration of isodose lines further aids users in their
 308 analyses. Furthermore, while organ doses are often rendered
 309 as non-intuitive tables or datasets, THUDose_{PD} revolution-
 310 izes this by offering three-dimensional visualizations of organ
 311 doses, enabling the display of specific organs to streamline
 312 user comparisons and in-depth analyses.

313 C. Validation of THUDose_{PD}

314 The program's accuracy in phantom dose assessment un-
 315 derwent rigorous testing in several scenarios. THUDose_{PD}
 316 was benchmarked against various ICRP publications, cover-
 317 ing areas, such as external photon irradiation, external neu-
 318 tron irradiation, and internal electron irradiation, to authen-
 319 ticate its physical processes and dose calculation method-
 320 ologies. Additionally, by transforming the Chinese refer-
 321 ence polygon-mesh phantom into voxels, discrepancies be-
 322 tween the voxelized phantom and the established benchmark
 323 were scrutinized. Given the program's reliance on a three-
 324 dimensional visualization platform, its prowess in depicting
 325 the geometry and results in 3D is also showcased.

326 1. Benchmark against ICRP publications

327 The external irradiation benchmarking leveraged insights
 328 from ICRP publication 116. This evaluation contrasted dose
 329 conversion coefficients for ISO irradiation with monoener-
 330 getic photons and AP irradiation with monoenergetic neu-
 331 trons. The internal irradiation benchmarking drew from the
 332 research of Zankl et al.[30, 31], which examined the SAF
 333 values of organs when subjected to electron and photon ir-
 334 radiation.

335 ICRP Publication 116 deduces reference conversion coef-
 336 ficients for both the effective dose and organ-absorbed doses
 337 under various external exposure conditions. This is based on
 338 the ICRP reference phantoms for both genders. It offers data
 339 from external beams of monoenergetic photons, electrons,
 340 positrons, and neutrons with configurations such as AP, PA,
 341 LLAT, RLAT, ROT, and ISO. In our assessment, the focus was
 342 on validating dose conversion coefficients specifically for the
 343 ICRP reference male, choosing monoenergetic photons and
 344 neutrons ranging from 10keV to 10GeV for the process.

345 Zankl et al. employed the ICRP reference male and the
 346 EGSnrc Monte Carlo program to deduce SAF values for pho-
 347 tons and electrons, considering varied source organs and tar-
 348 get organs. To ascertain the precision of SAF values derived
 349 using THUDose_{PD}, the ICRP reference male served as the
 350 basis for calculating the SAF values for electrons moving
 351 from the kidney to three distinct organs: the kidney itself, the
 352 adrenals, and the liver. The outcomes of this exercise were
 353 juxtaposed against Zankl's findings.

354 2. Polygon-mesh phantom voxelization

355 The polygon-mesh phantom was crafted by demarcating
 356 the organ boundaries of the voxel phantom using three-
 357 dimensional visualization software. This formed polygon
 358 mesh phantom boasts flexibility, allowing adjustments in
 359 height, weight, and posture. Once tailored, the modified
 360 polygon-mesh phantom was then imported into THUDose_{PD}
 361 for dose calculations by transforming it back into a voxel
 362 phantom. Illustrating this with the Chinese polygon mesh ref-
 363 erence male phantom (*CRAM_S*) as a case in point, the steps
 364 for voxelization can be seen in Figure 3.

365 First, the polygon-mesh phantom was adjusted using the
 366 three-dimensional modeling software Rhino to realize the tar-
 367 get size and posture. Layers were added and named for
 368 each organ. The Python plug-in of Rhino was used to write
 369 scripts for batch export based on the polygon mesh phantom
 370 in *.3dm form. Then, each organ was exported as an *stl* file
 371 with the same file name as the organ layer, and simultane-
 372 ously the *stl* file list was exported, i.e., *.lst text file, in which
 373 the file names are sorted from the largest to the smallest organ
 374 volume.

375 Subsequently, preparation of a phantom information file
 376 is necessary. This file should detail the index and antic-
 377 ipated weight of each organ. Moreover, during the post-
 378 processing phase of dose calculations — particularly when
 379 merging residual tissues — it is essential to identify the group

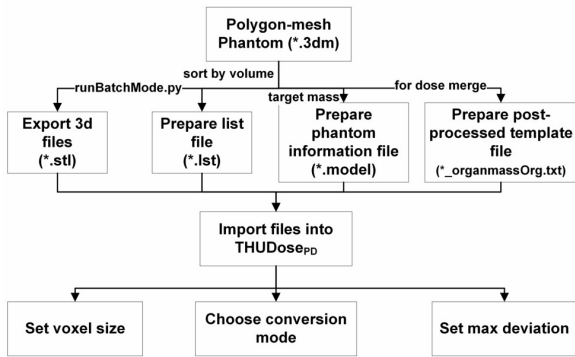


Fig. 3. Flow chart of the voxelization operation in *THUDose_{PD}*.

380 to which an organ belongs. This type of information is then
 381 saved in a text file, denoted as (*.organmassOrg.txt).

382 The previously prepared files were then loaded into
 383 *THUDose_{PD}*. Users can set their preferred voxel size, ex-
 384 pressed in millimeters (mm). Once the conversion mode is
 385 chosen, the program permits a maximum permissible devia-
 386 tion from the intended organ weight. It is worth noting that
 387 all organs are converted in descending order of size. Given
 388 this approach, conflicts may arise when smaller-volume or-
 389 gans intersect with larger ones. To address such conflicts, the
 390 program offers three resolution methods: overwriting, retain-
 391 ing, and randomizing.

392 **overwrite:** 'Overwrite' refers to the region where the
 393 conflict occurs is covered by the small volume organ that
 394 is converted later.

395 **keep:** 'Keep' denotes that the current conversion result is
 396 maintained, and the small volume organ that will be
 397 converted later avoids the conflict area.

398 **random:** 'Random' means that in conflict areas, small-
 399 volume organs are randomly covered.

400 The maximum deviation was used to ensure the upper limit
 401 of deviation between the voxelized organ mass and expected
 402 mass. The algorithm is realized by a loop that combines the
 403 corrosion and dilation algorithms. In this study, a polygon-
 404 mesh phantom *CRAM_S* with a height of 170 cm and weight
 405 of 63 kg was voxelized. In the *THUDose_{PD}* parameter con-
 406 figuration, the voxel resolution is 1.741mm × 1.741mm ×
 407 1.000mm, the conversion mode is selected as 'overwrite,' and
 408 the maximum deviation is set to 2%. The results of the output
 409 voxel phantom, *CRAM*, were compared for organ mass and
 410 tested for the efficiency of the entire conversion process.

3. Three-dimensional dose assessment

412 A three-dimensional depiction of an indoor work environ-
 413 ment was evaluated across several layers: the combined vi-
 414 sualization of ray traces with geometry, integrated display of
 415 phantom files with three-dimensional dose distribution, and
 416 independent portrayal of phantom organ doses.

417 For the ray trace and geometry visualization test, a new-
 418 born phantom undergoing radiography was used. This phan-
 419 tom was subjected to a vertebral photon beam in an AP con-
 420 figuration. The distance between the source and the phan-
 421 tom's back was set at 100 cm, with a radiation field measur-
 422 ing 12.5cm × 17.4cm. To examine the integrated visualiza-
 423 tion of phantoms with three-dimensional dose distributions,
 424 and the distinct portrayal of organ doses, an external irradia-
 425 tion scenario was simulated using an isotropic point source.
 426 The chosen phantom for this test was a reference Chinese
 427 adult male. Positioned directly in front of the phantom was
 428 a ¹³⁷Cs point source, emitting energy at 661keV. The three-
 429 dimensional dose distributions and organ doses were concur-
 430 rently scored and then utilized in the visualization tests.

III. RESULTS

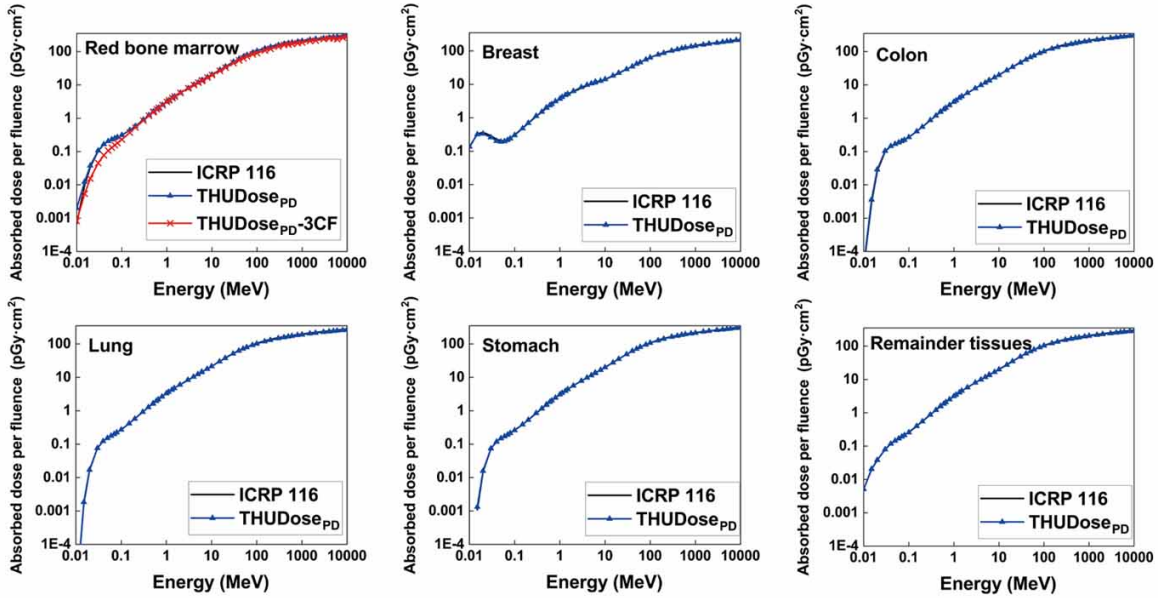
A. Benchmark against ICRP publication 116

433 In the study, *THUDose_{PD}* was employed to determine the
 434 absorbed dose of the ICRP reference male subjected to ISO
 435 geometry. We focused our analysis on radiation-sensitive or-
 436 gans with significant radiation weight factors. The dose cal-
 437 culation for the phantom was executed using 100 CPU cores,
 438 transporting 1E8 particles in a parallel manner. Figure 4 (a)
 439 displays the organ absorbed dose per fluence for 1E8 mo-
 440 noenergetic photons. Within this, both the 'Direct method'
 441 and '3CFs-improved method' were employed to assess the
 442 dose for the red bone marrow. These methods correspond to
 443 'THUDose_{PD}' and 'THUDose_{PD} – 3CF' in the legend, re-
 444 spectively. It is evident that our results align with the data
 445 from ICRP Publication 116. Notably, over 95% of our find-
 446 ings deviate from the ICRP Publication 116 data by less than
 447 5%. The remaining deviations, particularly in results with
 448 larger discrepancies, are predominantly attributed to substan-
 449 tial statistical errors in both datasets at lower energies. We
 450 further juxtaposed the results of red bone marrow dose calcu-
 451 lations using the 3CFs-improved method. This approach ef-
 452 fectively rectified the elevated values observed in direct cal-
 453 culation methods in lower-energy areas, as confirmed by a
 454 prior study[28].

455 Using analogous calculation parameters as applied for pho-
 456 tons, we determined the dose for neutrons irradiated with an
 457 AP geometry. Our focus was primarily on lung, skin, and
 458 brain tissues. Figure 4 (b) presents the absorbed dose per flu-
 459 ence for 1E8 monoenergetic neutrons. When juxtaposed with
 460 ICRP data, our findings exhibited consistency across a broad
 461 spectrum of energy levels, ranging from keV to GeV.

462 ICRP Publication 133 offers data pertinent to internal ex-
 463 posure, including SAF values deduced via the Monte Carlo
 464 method. This represents the proportion of radiant energy orig-
 465 inating from the source region that is absorbed per mass in the
 466 target region. Given that these ICRP data stem from Zankl's
 467 work, we reference them as 'Zankl et al.' in our subsequent
 468 analyses. Figure 5 (a) and Figure 5 (b) illustrate the SAFs
 469 of electrons and photons traveling from the kidney to various
 470 target organs, including the kidney itself, the adrenal glands,

(a) photon irradiation



(b) neutron irradiation

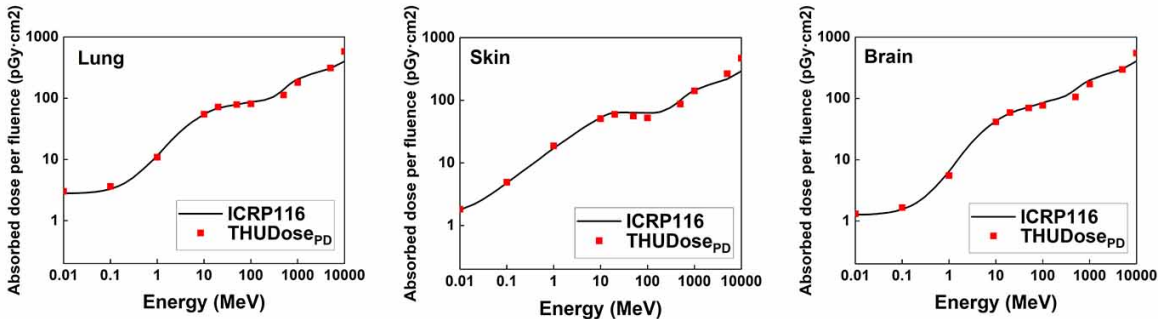


Fig. 4. (a) Organ absorbed dose per fluence for mono-energetic photons incident in ISO, (b) Organ absorbed dose per fluence for mono-energetic neutron incident in AP.

471 and the liver. When the kidney functioned as both the source
 472 and target, the relative deviation in SAF values was capped at
 473 3%. However, for target organs, such as the adrenal gland or
 474 liver, substantial deviations were observed at lower energies
 475 due to considerable statistical errors. Yet, the results closely
 476 matched at higher energy levels.

477 **B. Polygon-mesh phantom voxelization**

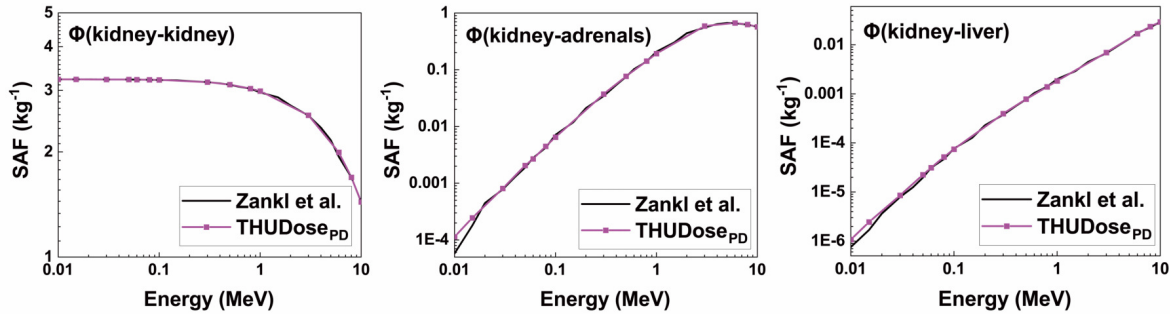
478 Upon voxelization of $CRAM_S$, we obtained the voxel
 479 phantom $CRAM$ with dimensions of [276, 156, 1700] and a
 480 cumulative count of 73195200 voxels. This encapsulates 103
 481 organs and tissues of the Chinese reference male. A com-
 482 parison of voxelization results with the ground truth values is
 483 depicted in Figure 6. The orange bars illustrate the genuine

484 value, which signifies the anticipated mass of the organ prior
 485 to voxelization. Conversely, the green bars indicate the post-
 486 conversion mass of the respective voxel, following the trans-
 487 formation from polygon-mesh organs. The relative deviation
 488 between these two, as showcased in Figure 6, aligns with the
 489 predetermined permissible deviation threshold of 2%.

490 Furthermore, we chose four phantoms from the Chinese
 491 adult standing phantom repository for the voxelization pro-
 492 cess. Their respective conversion durations are detailed in
 493 Table 1. The process to voxelize an adult phantom, contain-
 494 ing between 50 to 90 million voxels, spans approximately 2-3
 495 minutes, contingent on the phantom's size.

496 The resultant visualization file is outputted in the **.wrl* for-
 497 mat, allowing users to leverage any three-dimensional visual-
 498 ization software for analysis. This includes evaluating object
 499 coordinates, radiation field dimensions, and other pertinent

(a) electron irradiation



(b) photon irradiation

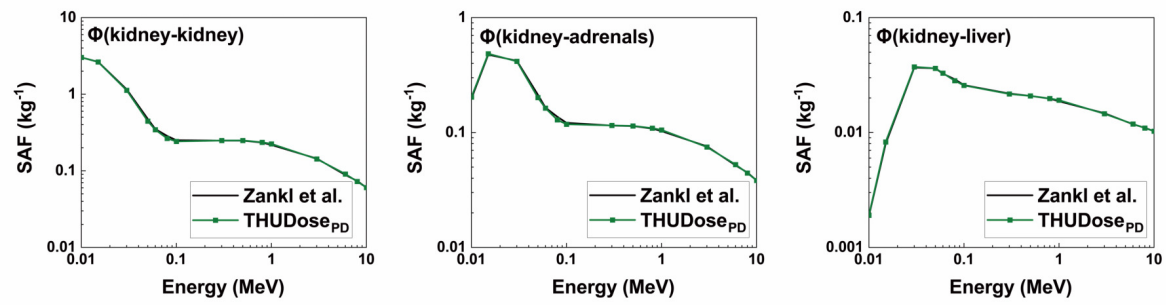


Fig. 5. (a) SAF values of electrons with kidney as the source organ, (b) SAF values of photons with kidney as the source organ.

500 data. The geometry and ray trajectories of neonatal phantom 501 tom radiographs focusing on the pelvis are presented in Figure 502 7 (a). Within THUDose_{PD}, the 'run parameter' dictates 503 whether the geometry is generated. If geometry generation is 504 approved, then the default history of transported particles is 505 set to ensure that the simulation scene can be rendered with 506 minimal computational effort. The amalgamation and display

Table 1. Voxelization cost time.

Phantom	Phantom size	conversion time (s)
H155M45	[258 146 1552]	120
H165M67	[282 168 1650]	150
H175M75	[288 184 1752]	156
H185M84	[294 176 1850]	196

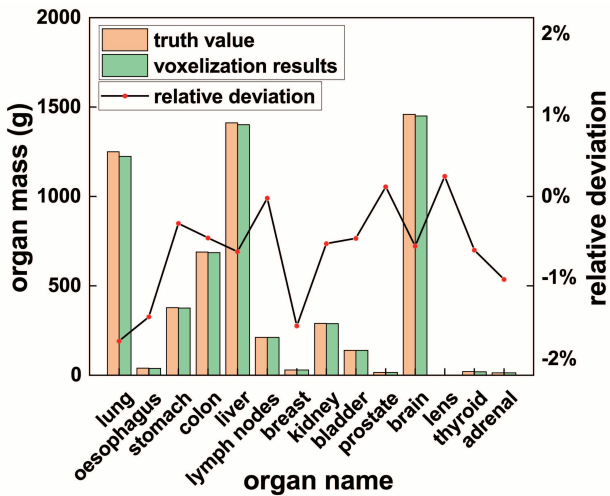


Fig. 6. Comparison of organ mass between voxelization results and truth values.

507 of tracks and geometries significantly streamline project 508 examinations.

509 Dose distribution within a phantom offers the most 510 straightforward approach to three-dimensional dose evalua- 511 tion. The amalgamation of the phantom and its three- 512 dimensional dose representation facilitates this methodology. 513 Figure 7 (b)-7 (c) illustrate the three-dimensional dose dis- 514 tribution from a ^{137}Cs point source utilizing an AP geom- 515 etry. Figure 7 (b) presents four distinct display modes of 516 the phantom and dose: (i) showcases the phantom's cross- 517 sectional view, (ii) emphasizes the dose distribution, (iii) in- 518 tegrates both phantom and dose visuals, and (iv) supple- 519 ments (iii) with isodose lines. This versatile visualization technique 520 assists users in analyzing radiation field metrics and dose lay- 521 outs. A comprehensive three-dimensional perspective, en- 522 compassing perspective, front, lateral, and top views comple- 523 mented by a color scale, is portrayed in Figure 7 (c).

524 Additionally, THUDose_{PD} introduces a feature for visu- 525 alizing the three-dimensional organ dose distribution. Figure

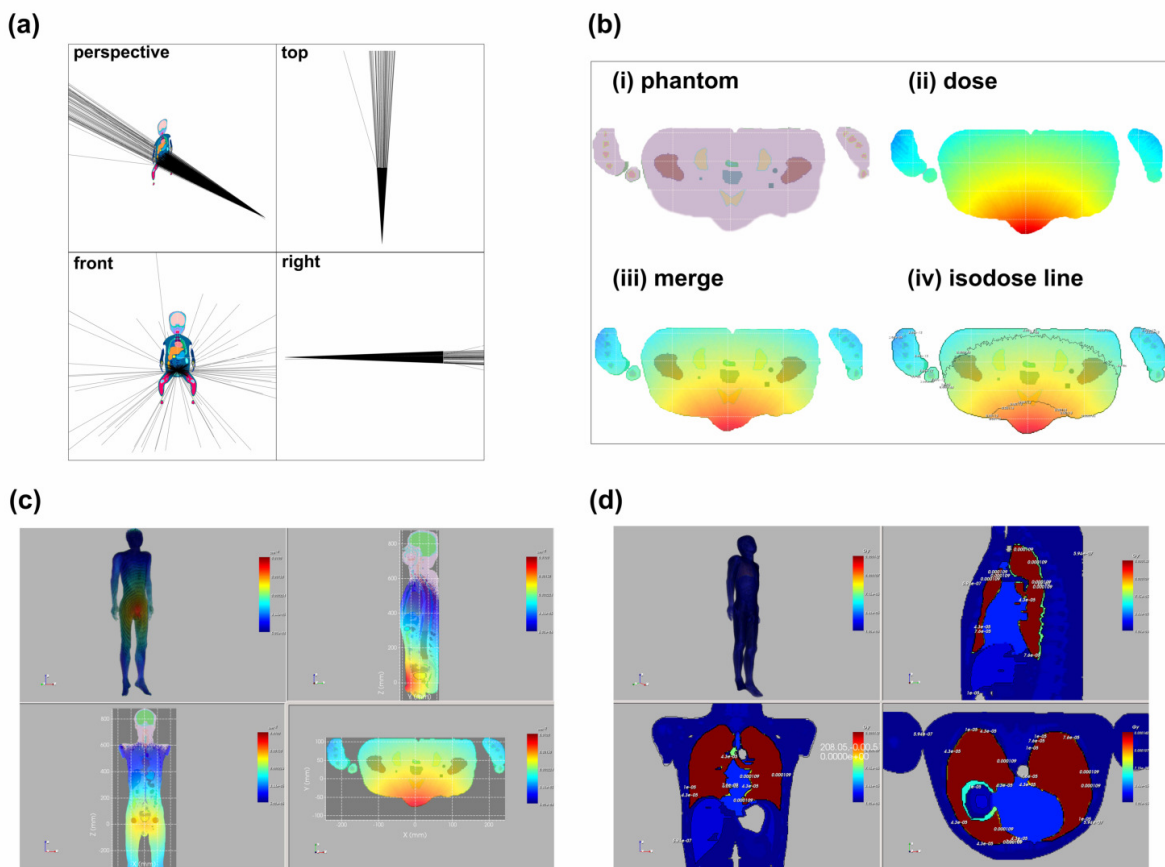


Fig. 7. (a) Geometry and track of neonatal pelvic X-ray photography, (b) Fused display of voxel phantom and three-dimensional dose distribution, (c) Three-dimensional dose distribution of isotropic point source irradiation with ^{137}Cs , (d) Three-dimensional organ dose of a random energy spectrum.

526 7 (d) displays the organ doses across various energy spectra. 527 Each organ's dose is represented by a distinct color, signifying 528 its specific dose amount.

529

IV. CONCLUSION

530 In this research, we introduced the Monte Carlo simula- 531 tion platform, THUDosePD, tailored for three-dimensional 532 phantom dose evaluations. This platform is adept at parallel 533 processing of photons, electrons, neutrons, and other parti- 534 cle types using both CPU and GPU. It offers a plethora of 535 methods for defining sources and geometries. Significantly, 536 it incorporates a voxelization technique for the polygon mesh 537 phantom, achieving phantom conversions with a precision un- 538

539 der 2% in approximately 2 min. Moreover, it supports calcu- 540 lations for both external and internal organ irradiation doses 541 and enables visualization of three-dimensional geometry, par- 542 ticle trajectories, and dose distributions. Catering to an array 543 of requirements in three-dimensional phantom dose assess- 544 ments, this platform proves invaluable for both radiation pro- 545 tection and clinical scenarios. Currently, its applications span 546 personal dose evaluations[32], environmental exposure dose 547 coefficients[27], internal radiation cancer risk studies, dosi- 548 metric reconstructions for a radiological mishap in Nanjing, 549 China[33], CT radiation dose evaluations[26, 34], and more, 550 underlining its substantial potential in the field.

551 [1] W.-M. Sun, N. Du, W.-D. Tian, and L. Wang, *Nuclear Science* 552 and *Techniques* **32**, 42 (2021).

553 [2] C.-Y. Li, X.-B. Xia, J. Cai, Z.-H. Zhang, G.-Q. Zhang, J.-H. 554 Wang, and Z.-C. Qian, *Nuclear Science and Techniques* **32**, 22 555 (2021).

556 [3] C.-M. Niu, M.-H. Li, and J.-R. Dai, *Nuclear Science and Tech-* 596
557 *niques* **32**, 12 (2021). 10.2172/1086758.

558 [4] Y. Wang, Y.-Y. Liu, B. Wu, X.-P. Meng, J.-P. Cheng, Y. Wang, 597
559 L.-J. Wang, Y.-S. Xiao, Q.-J. Cao, J.-F. Zhang, *et al.*, *Nuclear* 598
560 *Science and Techniques* **33**, 20 (2022). 599
561 [5] J.-Y. Chen, D.-Q. Wang, X.-D. Zhang, Q. Fu, X.-N. Yan, 600
562 K. Men, J.-R. Dai, and N. Bi, *Nuclear Science and Techniques* 601
563 **33**, 51 (2022). 602
564 [6] S.-C. Huang, H. Zhang, K. Bai, Y. Luo, H.-J. Mao, and Z.-Y. 603
565 Dai, *Nuclear Science and Techniques* **33**, 119 (2022). 604
566 [7] Z. Peng, N. Gao, B. Wu, Z. Chen, and X. G. Xu, *J. Radiat.* 605
567 *Prot. Res* **47**, 111 (2022). 606
568 [8] A. K. Hu, R. Qiu, H. Liu, Z. Wu, and R. J. Yang, *Nuclear Sci-* 607
569 *ence and Techniques* **32** (2021), 10.1007/s41365-021-00866-2. 608
570 [9] J.-L. Chen, S.-J. Yun, T.-K. Dong, Z.-Z. Ren, and X.-P. Zhang, 609
571 *Nuclear Science and Techniques* **33**, 11 (2022). 610
572 [10] D. Rogers, *Physics in Medicine & Biology* **51**, R287 (2006). 611
573 [11] G. Santin, D. Strul, D. Lazaro, L. Simon, M. Krieguer, M. V. 612
574 Martins, V. Breton, and C. Morel, *IEEE Transactions on nu-* 613
575 *clear science* **50**, 1516 (2003). 614
576 [12] S. Jan, D. Benoit, E. Becheva, T. Carlier, F. Cassol, P. Descourt, 615
577 T. Frisson, L. Grevillot, L. Guigues, L. Maigne, C. Morel, 616
578 Y. Perrot, N. Rehfeld, D. Sarrut, D. R. Schaart, S. Stute, 617
579 U. Pietrzik, D. Visvikis, N. Zahra, and I. Buvat, *Phys Med* 618
580 *Biol* **56**, 881 (2011). 619
581 [13] J. Perl, J. Shin, J. Schümann, B. Faddegon, and H. Paganetti, 620
582 *Medical Physics* **39** (2012), 10.1111/1.4758060. 621
583 [14] B. Faddegon, J. Ramos-Mendez, J. Schuemann, A. McNamara, 622
584 J. Shin, J. Perl, and H. Paganetti, *Physica Medica* **72**, 114 623
585 (2020). 624
586 [15] X. G. Xu, T. Liu, L. Su, X. Du, M. Riblett, W. Ji, D. Gu, C. D. 625
587 Carothers, M. S. Shephard, F. B. Brown, M. K. Kalra, and 626
588 B. Liu, *Annals of Nuclear Energy* **82**, 2 (2015). 627
589 [16] L. Su, Y. Yang, B. Bednarz, E. Sterpin, X. Du, T. Liu, W. Ji, 628
590 and X. G. Xu, *Med Phys* **41**, 071709 (2014). 629
591 [17] D. P. Adam, T. Liu, P. F. Caracappa, B. P. Bednarz, and X. G. 630
592 Xu, *Medical Physics* **47**, 2537 (2020). 631
593 [18] T. Goorley, M. James, T. Booth, F. Brown, J. Bull, L. J. 632
594 Cox, J. Durkee, J. Elson, M. Fensin, and R. A. Forster, 633
595 Los Alamos, NM: Los Alamos National Laboratory (2013), 634
596
597 [19] C. Ahdida, D. Bozzato, D. Calzolari, F. Cerutti, N. Charitonidis, 598 A. Cimmino, A. Coronetti, G. D'Alessandro, A. Donadon, 599 Serville, L. Esposito, *et al.*, *Frontiers in Physics* , 705
600 (2022). 601
601 [20] J. Allison, K. Amako, J. Apostolakis, H. Araujo, P. A. Dubois, 602 M. Asai, G. Barrand, R. Capra, S. Chauvie, R. Chytracek, 603 *et al.*, *IEEE Transactions on nuclear science* **53**, 270 (2006). 604
604 [21] L. Xi-yu, Q. Rui, W. Zhen, M. Rui-yao, Y. Shu-chang, Z. Hui, 605 and L. Jun-li, *MODERN APPLIED PHYSICS* **12**, 6 (2021). 606
606 [22] Y. S. Q. R. Z. H. L. J. WU Zhen, LU Wei, *Journal of Harbin 607
Engineering University* **43**, 9 (2022). 608
608 [23] G. Gualdrini and P. Ferrari, *Radiation Protection Dosimetry* 609
609 **143**, 125 (2011). 610
610 [24] W. Kainz, E. Neufeld, W. E. Bolch, C. G. Graff, H. K. Chan, 611 N. Kuster, B. Lloyd, T. Morrison, P. Segars, and Y. S. Yeom, 612
612 *IEEE Transactions on Radiation and Plasma Medical Sciences* 613
613 **3**, 1 (2019). 614
614 [25] Y. S. Yeom, J. H. Jeong, M. C. Han, and C. H. Kim, *Physics* 615
615 *in Medicine & Biology* **59**, 3173 (2014). 616
616 [26] R. Ma, R. Qiu, Z. Wu, L. Ren, A. Hu, W. B. Li, and J. Li, *Phys* 617
617 *Med Biol* **66** (2021), 10.1088/1361-6560/ac1ef1. 618
618 [27] W. Lu, R. Qiu, Z. Wu, C. Li, B. Yang, H. Liu, L. Ren, and 619
619 J. Li, *Phys Med Biol* **62**, 2276 (2017). 620
620 [28] L. Liu, Z. Zeng, J. Li, B. Zhang, R. Qiu, and J. Ma, *Physics* 621
621 *in Medicine & Biology* **54**, 6675 (2009). 622
622 [29] N. Petoussi-Henss, W. E. Bolch, K. F. Eckerman, A. Endo, 623 N. Hertel, J. Hunt, M. Pelliccioni, H. Schlattl, and M. Zankl, 624
624 *Annals of the Icrp* **39**, 1 (2010). 625
625 [30] M. Zankl, H. Schlattl, N. Petoussi-Henss, and C. Hoeschen, 626
626 *Physics in Medicine & Biology* **57**, 4501 (2012). 627
627 [31] J. E. Valentin, *Annals of the Icrp* **37**, 1 (2007). 628
628 [32] X. Luo, R. Qiu, Z. Wu, S. Yan, H. Zhang, and J. Li, *J Radiol* 629
629 *Prot* **43** (2023), 10.1088/1361-6498/acad0d. 630
630 [33] W. Lu, Z. Wu, R. Qiu, C. Li, B. Yang, S. Gao, L. Ren, and 631
631 J. Li, *Health Physics* **113**, 327 (2017). 632
632 [34] R. Li, Q. Rui, W. Zhen, M. Ruiyao, L. Junli, L. Chunyan, 633
633 S. Yinping, Z. Weiguo, and S. Quanfu, *Chinese Journal of* 634
634 *Radiological Medicine and Protection* **38**, 7 (2018).